RSC Advances

ROYAL SOCIETY OF CHEMISTRY

www.rsc.org/advances

Secondary Channels in the Thermal Decomposition of Monomethylhydrazine (CH_3NHNH_2)

Peng Zhang,[1*] Stephen J. Klippenstein,[2*] Lawrence B. Harding,[2] Hongyan Sun,[3] and Chung K. Law[3]

[1] Department of Mechanical Engineering

the Hong Kong Polytechnic University

Hong Kong

[2] Chemical Sciences and Engineering Division

Argonne National Laboratory

Argonne, Illinois 60439, USA

[3] Department of Mechanical and Aerospace Engineering

Princeton University

Princeton, New Jersey 08544, USA

* To whom correspondence should be addressed: pengzhang.zhang@polyu.edu.hk (Peng Zhang), sjk@anl.gov (Stephen J. Klippenstein)

Abstract

Mass spectrometric observations in a very low pressure pyrolysis study (Golden et al., Int. J. Chem. Kinet. 1972, 4, 433-448) of the decomposition of the prototypical rocket fuel monomethylhydrazine (MMH) indicated a dominant role for the molecular channels producing NH_3 and H_2 and their coproducts. In contrast, a recent ab initio transition state theory based master equation theoretical study (Zhang et al., Proc. Combust. Inst. 2011, 33, 425-432) indicated that simple N-N and C-N bond fissions dominate the kinetics. The possible role of molecular decomposition channels in MMH is explored further through additional investigations of the potential energy surface. These investigations consider the role of triplet channels, of roaming radical channels, and of some previously unexplored pathways for molecular decomposition. New ab initio transition state theory based master equation calculations provide revised predictions for the temperature and pressure dependence of the MMH decomposition kinetics that are in excellent agreement with recent shock tube measurements (Li et al., Comb. Flame 2014, 161, 16-22). These calculations continue to suggest only a very limited contribution from the molecular elimination channels. A roaming pathway is suggested to provide the dominant route for direct formation of ammonia. The possible role of secondary abstraction reactions in the very-low-pressure pyrolysis experiments is briefly discussed.

Keywords: Monomethylhydrazine, decomposition, transition state theory, intersystem crossing, roaming reaction, master equation

1. Introduction

Monomethylhydrazine (MMH) is a commonly used hypergolic propellant in rocket engines.[1, 2] Since MMH tends to exothermically decompose upon contact with a hot surface or an oxidizer, its thermal decomposition is an important consideration related to fuel stability and storability. Moreover, the decomposition of MMH is a necessary component of the detailed kinetic mechanism for MMH oxidization, which is required for the numerical simulation of rocket engine combustion.

A reaction mechanism for the thermal decomposition of MMH was developed by Sun and Law[3, 4] and then used to model the overall thermal decomposition rates of Eberstein and Glassman[5] at 750-1500 K and 1 atm. The mechanism was also extended to model the shock tube experimental data for MMH pyrolysis.[4, 6, 7] Based on these studies, the N—N and C—N bond fission reactions,

$$CH_3NHNH_2 \rightarrow NH_2 + CH_3NH \quad \text{(R1)}$$

$$CH_3NHNH_2 \rightarrow CH_3 + NHNH_2 \quad \text{(R2)}$$

were found to be the most important reactions in the thermal decomposition of MMH. In this mechanism, the Arrhenius pre-exponential factors of the rate coefficients of R1 and R2 were estimated from generic reactions and the energy barriers were evaluated from CCSD(T)/6-311++G(3df,2p)//MPWB1K/6-31+G(d,p) and CBS-QB3 calculations.[3, 4]

Subsequently, we provided a detailed theoretical kinetics analysis for the reactions R1and R2, and the related reverse barrierless radical-radical association reactions,[8]

$$NH_2 + CH_3NH \rightarrow CH_3NHNH_2 \quad \text{(R-1)}$$

$$CH_3 + NHNH_2 \rightarrow CH_3NHNH_2 \quad \text{(R-2)}$$

In this analysis, the capture rates for R-1 and R-2 were evaluated with variable reaction coordinate transition state theory (VRC-TST)[9-11] employing interaction energies determined directly from multireference electronic structure calculations. Predictions for the pressure dependence and product branching in the dissociation of CH_3NHNH_2 were then obtained by solving the master equation while incorporating the transition state information from the VRC-TST calculations.

These theoretical predictions, which employed an expression for the collisional energy transfer parameter $\langle\Delta E_{down}\rangle$ of $200(T/300)^{0.85}$ cm^{-1}, agreed well with the experimental data of Kerr et al.[12] A

recent shock tube study of Li et al.,[7] which measured NH_2 time profiles, found that the theoretical rates of Zhang et al.[8] are in reasonable agreement with their experimental data at various temperatures and pressures, but that a reduction of the rate of R1 by 40% (perhaps due to an overestimate of $<\Delta E_{down}>$) would effect a closer match. However, there are significant discrepancies between the theoretical results and the experimental data of Eberstein and Glassman[5] for the overall decomposition rates, which suggests that either additional decomposition channels or secondary reactions may play a role. Furthermore, the very low pressure pyrolysis study of Golden et al.[13] suggests a dominant role for formation of NH_3 and H_2.

The prior study of Sun and Law[3] provided a fairly complete CBS-QB3 based study of the potential energy surface (PES) for the decomposition of MMH. However, there are a few other possible channels that may have an effect on the overall decomposition rate of MMH and/or on the formation of products such as H_2, NH_3, and CH_4. Of particular interest are channels producing triplet products via intersystem crossing from the ground singlet state. Also, roaming radical channels in the N-N and C-N bond fissions would produce NH_3 and CH_4, respectively. Meanwhile, roaming radical channels in C-H and N-H bond fissions would yield H_2.

The motivation of the present study is to first explore such new reaction channels on the PES for MMH decomposition with *ab initio* electronic structure theory and then, as appropriate, predict the rate coefficients for these channels with transition state theory. These calculations allow us to further consider the interpretation of the available experimental data, such as those of Golden et al.[13]

In the following text, the theoretical methods employed in the present electronic structure, transition state theory, and master equation calculations will be summarized in Section 2. This summary will be followed by presentation and discussion of the results in Section 3.

2. Theoretical Methods

2.1. Potential Energy Surface

The geometric structures, vibrational frequencies, and zero-point energy (ZPE) for the primary stationary points on the PES were obtained via density functional theory, employing the Becke

three-parameter functional and the Lee-Yang-Parr correlation functional (B3LYP) with the 6-311++G(d,p) basis set.[14, 15] The corresponding intrinsic reaction paths for the transition states were also examined at the B3LYP/6-311++G(d,p) level. Higher level stationary point energies were obtained from restricted QCISD(T) (quadratic configuration interaction with singles doubles and perturbative inclusion of triples) calculations. These restricted QCISD(T) calculations employed the correlation-consistent, polarized-valence, triple-ζ (cc-pVTZ) and quadruple-ζ (cc-pVQZ) basis sets of Dunning[16, 17] and were extrapolated to the complete basis set limit (CBS)[18] via the expression E[QCISD(T)/∞] = E[QCISD(T)/cc-pVQZ] + {E[QCISD(T)/cc-pVQZ] - E[QCISD(T)/cc-pVTZ]}×0.6938. The B3LYP/6-311++G(d,p) vibrational frequencies were employed to determine the zero-point energy corrections. This QCISD(T)/CBS//B3LYP/6-311++G(d,p) method is also employed in the analysis of the torsional minima and barriers for all the stationary points.

The spin-forbidden reaction paths to CH_3NH_2 + ^3NH and NH_3 + $^3NCH_3$, have enthalpies of reaction that are much lower than that of R1, but were not considered in previous studies of the PES. One primary focus of the present work involves the determination of the kinetic relevance of these two spin-forbidden pathways. To form either of these sets of spin forbidden products, a hydrogen atom must first migrate between the secondary amine group and the terminal ammonia group to form either CH_3NH_2NH or CH_3NNH_3; these two MMH isomers have not been reported in previous studies. In each case, the products may then be formed by lengthening of the N—N bond until an intersystem crossing (ISC) with the triplet state is reached,

$$CH_3NH_2NH \xrightarrow{ISC} CH_3NH_2 + NH\ (X^3\Sigma^-) \quad \text{(R3)}$$

$$CH_3NNH_3 \xrightarrow{ISC} NH_3 + NCH_3\ (X^3A_2) \quad \text{(R4)}$$

The minimum point on the crossing seam (MSX) between the singlet and triplet PESs for R3 and R4 plays a role analogous to the transition state in determining the contribution to the dissociation kinetics from these channels.[19, 20] Several methods have been proposed for determining

the MSX.[21-24] The MOLPRO quantum chemistry program package,[25] which was the primary resource for the electronic structure aspects of the present work, allows for the determination of the MSX with the complete active space self-consistent field (CASSCF) method.

Although the CASSCF method provides a good description of the multi-reference character of wave functions, it does not provide highly accurate energies due to its inadequate treatment of dynamical electron correlation. Thus, we have also evaluated the singlet and triplet energies at the CASSCF MSX geometries with the QCISD(T) method, which is expected to provide more accurate energies. Furthermore, on the singlet surface, lengthening of the N—N bond correlates with the formation of a singlet diradical, which often is not well described with single reference based methods such as the QCISD(T) method. Consequently, we have also used the complete active space with second-order perturbation theory (CASPT2) and multi-reference configuration interaction (MRCI) methods to explore the crossings. In these multi-reference calculations we have minimized the square of the singlet triplet energy difference, starting from geometries near the CASSCF MSX. Although these minimizations do not provide minimum points on the seam of crossing, they do provide geometries that are on the seam of crossing for the higher level method, and which are near to the CASSCF MSX geometry. As such, they likely provide a reasonable estimate of the true MSX geometry and energy. A two-electron, two-orbital, (2e,2o) complete active space, which consists of the pair of radical electrons on the triplet NH or NCH_3 radicals, was used in these calculations as the reference wave function.

For the N-N bond fission reaction there is also a roaming radical mediated pathway that leads to the production of $CH_2NH + NH_3$. The full roaming mediated reaction involves the sequence $CH_3NHNH_2 \rightarrow CH_3NH\ldots NH_2 \rightarrow CH_2NH + NH_3$, where $CH_3NH\ldots NH_2$ denotes a long-range hydrogen bonded complex separating MMH from $CH_2NH + NH_3$. The rovibrational and energetic properties of this roaming pathway were studied with the CASPT2 approach employing a (2e,2o) active space. The active space for these calculations consists of the radical orbitals of NH_2 and of CH_3NH. The cc-pVQZ basis set was used in exploring the roaming saddle point, the aug-cc-pVTZ basis set was used in predicting the properties for the other stationary points, the cc-pVTZ basis set

was employed in calculations along an NH distinguished reaction coordinate for the abstraction portion of the pathway, and the aug-cc-pVDZ basis set was used in the illustrative global mapping of the long-range interactions between CH_2NH and NH_3.

In the present study, all the density functional theory calculations were performed with the Gaussian program package,[26] while the MOLPRO program package[27] was used to perform all of the CASSCF, CASPT2, MRCI and QCISD(T) calculations.

2.2 High Pressure Kinetics

For the reaction channels with a large energy barrier, and thus a well-defined transition state, the high-pressure rate coefficients were obtained from transition state theory (TST) employing rigid-rotor harmonic-oscillator (RRHO) assumptions for all degrees of freedom except the torsional ones. Tunneling corrections based on asymmetric Eckart potentials were included. Hindered rotor corrections for the torsional modes were obtained from one-dimensional fits to the torsional potentials employing Pitzer-Gwinn like approximations and the $I^{(2,3)}$ moments of inertia.[28] The fits to the torsional potentials were designed to reproduce the B3LYP/6-311++G(d,p) torsional frequency at the minimum as well as the QCISD(T)/CBS//B3LYP/6-311++G(d,p) torsional barrier heights and secondary minima, if they exist. For R1 and R2, the VRC-TST analysis from Zhang et al.[8] was employed.

Theoretical frameworks for predicting the intersystem crossing (ISC) rate have been presented.[29, 30] However, these methods are somewhat involved and so it is worthwhile to consider alternatives. For example, experimental observations can sometimes be used to derive ISC rates from empirical fits to the data,[31, 32] or alternatively they can demonstrate that the ISC is insignificant.[33] It will be demonstrated in the next section that the MSXs for R3 and R4 have higher energy thresholds than the transition state for R1 and hence are expected to have a negligible influence on the decomposition rate of MMH. They are also expected to have a limited role in product formation. As a result, R3 and R4 were not considered in the present rate calculations.

2.3 Pressure Dependent Kinetics

As will be seen shortly, the PES for MMH decomposition consists of multiple, interconnected potential wells and multiple product channels. However, the particular form of this PES (i.e., the dominance of the decomposition from the CH_3NHNH_2 well to bimolecular products, even in the high pressure limit) allows for simplification to a single-well, multiple-channel one. The pressure dependent rate coefficients for this single well model were determined by solving the master equation. The relevant theory will not be discussed here since it has been described in detail in the literature[34, 35] and implemented in the VARIFLEX code.[36]

Following our previous study,[8] we employ a Lennard-Jones collision model and the energy transfer probability was approximated with a single-exponential-down model and an average downward energy transferred parameter, $<\Delta E_{down}>$, that is proportional to $T^{0.85}$. The approximation that $<\Delta E_{down}>$ increases roughly linearly with temperature has been validated in related studies such as that for the dissociation of C_2H_3 and C_2H_5[37] with the light bath gas molecules He, Ar, and N_2. The Lennard-Jones parameters for the MMH molecule are σ = 4.4 Å and ε = 340 cm^{-1}, which are based on the empirical method proposed by Wang and Frenklach.[38] For N_2, which was employed as the primary bath gas, we used σ = 3.62 Å and ε = 68 cm^{-1} [39] and the value of $<\Delta E_{down}>$ at room temperature was taken to be 120 cm^{-1}. In order to compare with the recent experimental data of Li et al.[7], Ar was also used as the bath gas with σ = 3.47 Å, ε = 79 cm^{-1} and a slightly larger room temperature $<\Delta E_{down}>$ of 130 cm^{-1}.[39] We also performed calculations for toluene as a bath gas since it is in high concentration in the toluene-carrier flow system of Kerr et al.[12] For toluene we employed Lennard-Jones parameters of σ = 4.7 Å and ε = 150 cm^{-1}. Due to the larger size of toluene, with many vibrational modes, one expects greater $<\Delta E_{down}>$ values for its collisions with MMH and for it we explore the effect of varying the room temperature $<\Delta E_{down}>$ value from 300 to 600 cm^{-1}.

2.4 Roaming Radical Kinetics

Kinetic predictions for the roaming radical pathway were obtained by treating the long-range $CH_3NH\ldots NH_2$ complex as a second well with exit channels to (i) the abstraction products, (ii)

$CH_3NH + NH_2$ and (iii) back to CH_3NHNH_2. A master equation based treatment of the decomposition then yields a predicted branching between formation of either $CH_3NH + NH_2$ or $CH_2NH + NH_3$. The requisite microcanonical rates for the abstraction channel are obtained from an RRHO based variational TST treatment employing a distinguished NH coordinate. The roaming saddle point correlates with the starting point of this variational pathway. The dissociation part of the analysis is performed with VRC-TST employing CASPT2(2e,2o)/aug-cc-pVDZ sampling and a one-dimensional correction to the CASPT2(2e,2o)/aug-cc-pVTZ level.

3. Results and Discussion

3.1 Potential Energy Surface for CH_3NHNH_2 Decomposition

The PES for MMH dissociation calculated at the QCISD(T)/CBS//B3LYP/6-311++G(d,p) level is shown in Figure 1. The optimized geometries for the stationary points on the PES and the corresponding frequencies and rotational constants are listed in the Supporting Information. Note that only the reaction channels that are directly connected to MMH and that also have relative energies less than 80 kcal/mol are included. Compared to the CBS-QB3 energies used in the previous study,[3] the QCISD(T)/CBS energies are about 0.5-2.0 kcal/mol lower. Recognizing that the present QCISD(T)/CBS method employs a much larger basis set for the QCISD(T) calculation, and thereby removes various additivity assumptions, this method is generally expected to be more accurate than the CBS-QB3 method. Sample comparisons with experiment for related systems indicate that the QCISD(T)/CBS predictions have uncertainties of about 1 kcal/mol even for the transition states. In the present work, the QCISD(T)/CBS energies were used in the rate coefficient calculations.

The PES employed in the VRC-TST calculations of the barrierless radical-radical association reactions R-1 and R-2 was described in detail in Zhang et al.[8] and hence will be only briefly summarized here. In the VRC-TST calculations, the intermolecular degrees of freedom of the fragments are treated as fully coupled anharmonic modes via classical phase space integrals. The interaction potential for these degrees of freedom was determined with on-the-fly CASPT2 calculations[40] employing the aug-cc-pVDZ basis set. These calculations employed the minimum

active space for properly describing the separated fragments, namely two electrons in two orbitals, (2e, 2o). Two orientation-independent correction terms were also included in the final PES to account for effects of increasing the basis set from aug-cc-pVDZ to aug-cc-pVTZ, and of relaxing the internal structure of the reacting fragments along the minimum energy path.

Besides the simple bond scission reactions R1 and R2, decomposition of MMH can also proceed via three-center, four-center, five-center, and roaming+abstraction transition states to different isomers and bimolecular products, as shown in Figure 1. Intramolecular transfer of a primary amine H atom to the central NH group via the three-center transition state TS1 yields CH_3NH_2NH,

$$CH_3NHNH_2 \rightarrow CH_3NH_2NH \quad (R5)$$

Similarly, intramolecular transfer of a secondary amine H atom to the terminal NH_2 group via TS2 yields CH_3NNH_3,

$$CH_3NHNH_2 \rightarrow CH_3NNH_3 \quad (R6)$$

These isomers can undergo further decomposition reactions, which will be discussed shortly.

In the previous study,[3] two H_2 elimination reaction paths via four-center transition states were found to have energy barriers of 106.9 kcal/mol and 108.7 kcal/mol, respectively. Here, a new H_2 elimination reaction path was explored

$$CH_3NHNH_2 \rightarrow CH_2NHNH + H_2 \quad (R7)$$

It involves a five-center transition state, TS3, with an energy barrier of 61.6 kcal/mol, which is actually 1.1 kcal/mol lower than that of R1. However, TS3 contains a five-member-ring and thus has a relatively low entropy due to the loss of all the internal rotors. Nevertheless, R7 holds the potential to be a kinetically important channel for direct H_2 formation. Another new H_2 elimination pathway

$$CH_3NHNH_2 \rightarrow CH_3NHN + H_2 \quad (R8)$$

involving a three-center transition state, TS6, was also explored. Although the energy barrier for TS6 is 10 kcal/mol higher than that for TS3, it has a larger entropy than that of TS3, and hence R8 may compete with R7 at higher temperatures.

As discussed in the previous study,[3] the intramolecular transfer of the H atom from the secondary amine group in MMH to the methyl group via a three-center transition state (TS4) yields

$CH_4 + NNH_2$, with an energy barrier of 66.1 kcal/mol. Furthermore, the migration of the H atom from the methyl group to the terminal amino group in MMH via a four-center transition state TS5 yields the products CH_2=NH + NH_3 with an energy barrier of 69.3 kcal/mol. The corresponding reaction paths are denoted by

$$CH_3NHNH_2 \rightarrow CH_4 + NNH_2 \quad \text{(R9)}$$

$$CH_3NHNH_2 \rightarrow CH_2{=}NH + NH_3 \quad \text{(R10)}$$

Since TS4 and TS5 have energies higher than that of R1, and are tighter, these reaction channels are not likely to make a significant contribution to the rate of MMH decomposition. However, they may provide the dominant pathways for CH_4 and NH_3 formation.

The N-N bond fission in CH_3NHNH_2 proceeds through a region of configurations corresponding to weakly interacting CH_3NH and NH_2 radicals. These radicals may reorient to place the NH_2 closer to the C side of the CH_3NH radical. From this side, there is a barrierless abstraction path to form NH_3 + CH_2NH. The plots in Figures 2 and 3 provide two separate illustrations of these long-range interactions. The contour plot (Figure 2) illustrates the interaction between the CH_3NH and NH_2 fragments for the N of NH_2 in the NCH plane and the HNCH torsion of CH_3NH roughly perpendicular to that plane. This plot indicates the presence of front and backside addition paths to form CH_3NHNH_2 (on the top and bottom left), an abstraction path to form CH_2NH + NH_3 (on the bottom right), and a roaming saddle point (at about y=4, z=0). The plot in Figure 3 projects the interaction energy onto the plane for an NH_2 group moving about the CH_3NH at a fixed separation of 3.5 Å, but with the CH_3NH now rotated so that the HNCH is in the plane of the plot. The addition paths now correlate with the black regions surrounding the N. The H that gets abstracted now lies out of the plane of the plot. The abstraction path then appears as the black region to the upper right of the C. The roaming dividing surface now shows up as the more or less vertical purple ridge passing through the C atom, with the roaming saddle point just above the C atom.

The fully optimized roaming saddle point for the reorientational motion, which is shown in Figure 4, lies 1.2 kcal/mol below the threshold for forming NH_2 + CH_3NH. The roaming radical pathway provides the lowest energy route for decomposition and, at low enough temperatures, it

provides the dominant decomposition path. At higher temperatures, entropic factors become more important and its role is reduced.

3.2 Potential Energy Surface for CH_3NH_2NH Decomposition

The CH_3NH_2NH isomer can also undergo further H_2 and CH_4 elimination to form products of diazenes and methyl diazenes, as shown in Figure 5. For clarity, only the channels leading to the lower energy isomers of diazene and methyl diazene are shown in the figure. It is seen that the energies of their corresponding transition states, TS1H and TS1M, are too high for them to be the dominant pathways for MMH decomposition, although they may contribute to the formation of H_2 and CH_4, respectively. CH_3NH_2NH can also undergo N—N bond fission to form CH_3NH_2 + NH. The dissociation limit for formation of CH_3NH_2 + NH($a^1\Delta$) radical is 29.8 kcal/mol above the products of R1. However, the singlet-triplet ($^1\Delta$-$^3\Sigma$) splitting of 35.9 kcal/mol[41] implies that CH_3NH_2 + NH($X^3\Sigma^-$) is at 56.6 kcal/mol, well below the CH_3NH + NH_2 threshold. The contribution of this triplet channel R3 depends on the rate of intersystem crossing.

To locate the minimum singlet-triplet crossing point for R3, we first examined the minimum energy paths for $CH_3NH_2NH \rightarrow CH_3NH_2$ + NH on both the singlet and triplet PESs at the CASPT2(2e,2o)/aug-cc-pVDZ level, as shown in Figure 6. The zero of energy in this plot corresponds to separated CH_3NH_2 + ^{3}NH. The singlet and triplet potential curves cross each other at an N—N bond length of 1.98 Å, where the energy is about 72.0 kcal/mol relative to CH_3NHNH_2. The approximate crossing geometry for the singlet state was used as an initial guess in searching for the MSX.

Figure 7(a) shows the geometry of the MSX at the CASSCF/6-311++G(d,p) level. The QCISD(T)/CBS energy for the singlet and triplet states at this geometry are 69.3 kcal/mol and 77.7 kcal/mol, respectively. Notably, the T1 diagnostics for both states are quite small, being only 0.022 and 0.017 for the singlet and triplet states, respectively, implying only weak multireference effects

for this geometry. Unfortunately, the 8 kcal/mol difference between the two QCISD(T) energies implies some dependence of the crossing geometry on dynamical correlation effects.

To explore this effect, geometries on the CAS+1+2+QC(2e,2o)/aug-cc-pVDZ crossing surface were found for a range of NN separations, as described in Sec. 2. The minimum of these crossing points was located at R_{N-N}=2.07 Å and the geometry (cf. Figure 7(b)) is very similar to the CASSCF geometry. Notably, at this geometry the QCISD(T)/CBS energies for the singlet and triplet states are much closer, being 75.3 and 72.4 kcal/mol, respectively. These observations suggest that the proper crossing point is likely at an energy of about 74 kcal/mol, with an uncertainty of perhaps 5 kcal/mol. Since this estimate for the MSX energy is more than 10 kcal/mol higher than the threshold for R1, the spin-forbidden channel R3 is unlikely to be kinetically significant. Thus, it will not be considered in the present rate calculations. This result is consistent with the observation of Golden et al.,[13] that there is no indication of CH_3NH_2 in their very low pressure pyrolysis (VLPP) experiments, in which the radical-radical routes for CH_3NH_2 formation, such as $CH_3 + NH_2 \rightarrow CH_3NH_2$, were suppressed.

3.3 Potential Energy Surface for CH_3NNH_3 Decomposition

The CH_3NNH_3 isomer can undergo an H_2 elimination reaction to form CH_2NNH_2, as shown in Figure 8. The energy of the corresponding transition state, TS2H-a, is higher than the dissociation limits of R1 and R2 and consequently unlikely to be kinetically important. Another H_2 elimination reaction of CH_3NNH_3 forms methyl diazene. The energy of the corresponding transition state, TS2H-b, is too high to be kinetically important.

For CH_3NNH_3, the N—N bond fission yields NH_3 and an NCH_3 radical, where the ground state of NCH_3 is again a triplet. The dissociation limit for the formation of the $NCH_3(X^3A_2)$ radical is only 40.8 kcal/mol. This value indicates that the reaction R4 may also be an important channel for MMH decomposition and NH_3 formation. The singlet-triplet adiabatic energy separation of 31.2 kcal/mol[42] again implies that the corresponding singlet products are kinetically inaccessible.

Following the same approach used to study R3, we first examined the minimum energy paths for $CH_3NNH_3 \rightarrow NH_3 + NCH_3$ on both the singlet and triplet PESs at the CASPT2(2e,2o)/aug-cc-pVDZ

level, as shown in Figure 9. In this plot the zero of energy now corresponds to separated NH_3 + $^3NCH_3$. The singlet and triplet potential curves cross each other at an N—N bond length of 1.92 Å, where the energy is about 65.8 kcal/mol relative to CH_3NHNH_2. The approximate crossing geometry for the singlet state was used as an initial guess in searching for the MSX.

Figure 10(a) shows the geometry of the MSX at the CASSCF/6-311++G(d,p) level. The QCISD(T)/CBS energies for the singlet and triplet states are 65.5 kcal/mol (T1 diagnostic = 0.018) and 72.1 kcal/mol (T1 diagnostic = 0.016), respectively. The location of CAS+1+2+QC(2e,2o)/aug-cc-pVDZ crossing points as a function of R_{N-N} again yields geometries (c.f. Figure 10(b)) that are very similar to the CASSCF geometry. The corresponding splitting between the QCISD(T)/CBS singlet and triplet energies, which are now 67.8 and 72.0 kcal/mol, is again reduced. These observations suggest that the proper crossing point is likely at an energy of 70±5 kcal/mol and, once again, this spin-forbidden channel is unlikely to be kinetically significant for MMH decomposition. Thus, it will not be considered in the following rate calculations.

3.4 High Pressure Kinetics of MMH Decomposition

For the barrierless R-1 and R-2 reactions, high pressure rate coefficients were calculated previously[8] with the VRC-TST method,[10, 11, 43] and then were converted to high pressure dissociation rate coefficients via computation of the equilibrium constant. The temperature dependence of the high-pressure decomposition and isomerization rate coefficients for MMH is shown in Figure 11. The fits of the high-pressure rate constants over the temperature range of 400-2500 K by the modified Arrhenius function are listed in Table 1.

Several useful observations about these rate calculations can be made. First, the two simple bond fission channels, especially R1, dominate the decomposition and isomerization kinetics of MMH over the entire temperature range of interest. This result implies that other channels have only secondary contributions to the total decomposition rate. Second, although the isomerization reaction R5 and the hydrogen elimination reaction R7 have slightly lower thresholds than R1, their decomposition rates are much smaller than those of R1 and R2 due to their tighter transition states.

Third, the increasing importance of the CH_4 elimination reaction R9 with temperature implies that it may be an important channel for CH_4 formation at high temperatures. Finally, the hydrogen elimination rate of R7 is generally much larger than that of R8, which however becomes comparable to the former at higher temperatures due to its looser transition state structure, as discussed in Section 3.1.

3.5 High Pressure Kinetics of NH_3 Formation

In the VLPP experiments of Golden et al.,[13] the product peaks at 17 amu (NH_3) and 2 amu (H_2) were used to compute total rate constants and the branching fraction for the formation of ammonia. The observation of only a small effect upon adding NO_2 to the mixture, was taken to indicate the absence of any radical products. It was then proposed that ammonia is formed via the four-center deamination reaction R10.

In VLPP experiments, collisions with a bath gas are replaced with wall collisions. This replacement makes it difficult to directly compare master equation predictions with VLPP data. Golden et al. obtained a high-pressure rate coefficient of $10^{13.2-54000/2.3RT}$ s^{-1} for the reaction by fitting RRKM and RRK calculations to the predictions. There are two aspects of these indirect results that are strongly discordant with the present calculation, as seen in Figure 12. First, the predicted rate constant for NH_3 formation exceeds our high pressure rate constant for R10 by at least two orders of magnitude. Such a large disagreement cannot be explained by considering the contribution from the other NH_3 forming channel, R5, because its NH_3 formation rate is still much smaller than the experimental data even if we assume all of the CH_3NNH_3 decomposes to $^3CH_3N + NH_3$. Second, their NH_3 formation rate coefficient roughly corresponds to their estimated total rate coefficient, which is about two orders of magnitude lower than our predicted rate for channel R1.

Interestingly, a roaming radical pathway[44, 45] for forming $NH_3 + CH_2$=NH via

$$CH_3NHNH_2 \rightarrow NH_2 \cdots CH_3NH \rightarrow NH_3 + CH_2{=}NH \qquad \text{(R11)}$$

provides a plausible explanation for an increased NH_3 formation rate. In this pathway, as the N—N bond of MMH stretches, the NH_2 radical starts roaming around the CH_3NH radical and sampling

large volumes of the orientation space. The roaming channel opens up when the incipient radicals sample orientations leading to the barrierless hydrogen abstraction forming NH_3 + CH_2=NH. The present calculations suggest that the roaming radical channel contributes between 1.5 and 2.5% of the N-N bond fission rate for temperatures ranging from 500 to 2000 K and pressures ranging from 0.0013 atm to 100 atm. This fraction increases dramatically with decrease in temperature below 500 K reaching about 50% at 100 K, but little dissociation occurs at such low temperatures. Notably, in the 1000 K range this contribution to the NH_3 formation rate is reasonably close to the value estimated by Golden et al.[13] We expect considerable uncertainty (e.g., a factor of 5) in this prediction of the roaming contribution due to our use of harmonic oscillator assumptions for the roaming transition state.

The NH_3 in the VLPP experiment could alternatively be attributed to a hydrogen abstraction reaction of NH_2 from CH_3NHNH_2. Such radical-molecule reactions, which are generally considered to be suppressed in VLPP, will be discussed in the next section.

3.6 High Pressure Kinetics of H_2 Formation

A large amount of hydrogen was found in the experiment of Golden et al.[13] and proposed to be produced from the reaction MMH → CH_3N=NH + H_2 via a four-center transition state. Their high-pressure rate coefficient, $10^{13.5-57000/2.3RT}$ s^{-1}, for this reaction was again obtained by fitting their experimental results to predictions from RRKM and RRK theories. As shown in Figure 13, neither the individual reactions R7 and R8 nor their combinations are sufficient to explain the estimates of Golden et al. For the channel proposed by Golden et al., MMH → CH_3N=NH + H_2, the presently calculated energy for its transition state is about 35-45 kcal/mol higher than that of R7 and R8, as discussed in Section 3.1. As a result, the rate coefficient of MMH → CH_3N=NH + H_2 is simply too small to be kinetically important for hydrogen formation. By the same token, the reactions MMH → CH_3NH_2NH → CH_3N=NH + H_2, MMH → CH_3NNH_3 → CH_2NNH_2 + H_2, and MMH → CH_3NNH_3 → CH_3N=NH + H_2 have negligible contributions to hydrogen formation due to their high energy transition state barriers and therefore small rate coefficients, as already seen in Figures 5 and 8.

Sun and Law[3] reported three barrierless reaction channels for H radical elimination, namely

$$CH_3NHNH_2 \rightarrow CH_3NNH_2 + H \quad \text{(R12)}$$

$$CH_3NHNH_2 \rightarrow CH_3NHNH + H \quad \text{(R13)}$$

$$CH_3NHNH_2 \rightarrow CH_2NNH_2 + H \quad \text{(R14)}$$

In the present study, we repeated the geometry optimization and the higher level energy calculation for R12-R14, among which R12 was found to have the smallest dissociation energy, which is 78.3 kcal/mol at the QCISD(T)/CBS//6-311++G(d,p) level, as compared to the 79 kcal/mol reported in Sun and Law.[3] Furthermore, the dissociation energies of R13 and R14 were found to be 2.4 kcal/mol and 13.6 kcal/mol higher than that of R12, respectively.

To examine the possible significance of the roaming channel MMH → CH_3NNH_2 + H → $CH_2NNH_2 + H_2$ for hydrogen formation, we made the following rough estimation of the upper bound for the dissociation rate of R12. First, we assumed the reverse reaction of R12 has an association rate constant of 4×10^{-10} cm^3 $molecule^{-1}$ s^{-1}, which should be an upper bound for all relevant temperatures and pressures. The dissociation rate can be estimated by using the association rate and an accurately calculated equilibrium constant. As seen in Figure 13, the estimated dissociation rate for R12 is substantially smaller than the experimental data by a factor of 10-100 for temperatures between 900-1200 K. The branching ratio of a roaming induced abstraction channel to the radical-radical dissociation channel is generally much less than unity (typically 10% or less) in this temperature range. Thus, the roaming channel cannot explain the large amount of H_2 formation in the experiment of Golden et al.[13]

Since we have now ruled out all the possible hydrogen formation channels on the PES of MMH decomposition, we reconsider the possibility of hydrogen formation via radical-involved secondary reactions, which are generally believed to be insignificant in the VLPP experiment. The most likely radical-molecule reactions for hydrogen formation are the hydrogen abstraction reactions

$$H + CH_3NHNH_2 \rightarrow CH_3NNH_2 + H_2 \quad \text{(R15)}$$

$$H + CH_3NHNH_2 \rightarrow CH_3NHNH + H_2 \quad \text{(R16)}$$

$$H + CH_3NHNH_2 \rightarrow CH_2NHNH_2 + H_2 \quad \text{(R17)}$$

where the hydrogen radical would likely come from the decomposition of the CH_3NH radical.

An analysis of the relative importance of radical-molecule reactions in the VLPP experiment of Golden et al.[13] is given in the Appendix. A critical rate constant, $k_{M,cr} = 3.2\times10^{-12}$ cm^3 molecule^{-1} s^{-1}, was derived based on the experimental condition of about 4×10^{-5} torr pressure and typical temperature of 1000 K. Based on the analysis, a radical-molecule reaction cannot be neglected in their experiment if its bimolecular reaction rate is close to or larger than the critical value.

The CCSD(T)/6-31+G(d,p)//MP2(full)/6-31+G(d,p) based *ab initio* transition state theory predictions of Sun and Law[3] for R15 – R17 indicate that only the rate coefficient for R15, which is about 7.94×10^{-13} cm^3 molecule^{-1} s^{-1} at 1000 K, is close to the critical rate constant and therefore holds potential importance to hydrogen formation. However, a reexamination of these rate coefficients at the QCISD(T)/CBS//B3LPY/6-311++G(d,p) level by Sun et al.[46] yields much larger rate coefficients of 5.5×10^{-12}, 4.7×10^{-12}, and 2.5×10^{-12} cm^3 molecule^{-1} s^{-1}, for R15, R16, and R17 respectively, which are all comparable to $k_{M,cr}$. Consequently, R15-R17 each hold the potential to be important in interpreting the hydrogen formation in the VLPP experiment and merit further study in modeling the experiment.

Sun and Law also predicted the rate coefficients for hydrogen abstraction reactions of MMH by the NH_2 radical.[3] Their predictions indicate that the highest rate coefficient for these reactions, corresponding to the attack of NH_2 to the central amine hydrogen, is about 2.0×10^{-13} cm^3 molecule^{-1} s^{-1} at 1000 K, which is well below the critical value. Cook et al. increased the rate by a factor of 10 to fit their measured NH_2 and NH_3 time history.[6] However, such a modification was not supported by a reexamination of the rate at the QCISD(T)/CBS//B3LPY/6-311++G(d,p) level by Sun et al.[46] Consequently, the contribution to ammonia formation from these reactions is presumed negligible here. This expectation provides support for our suggestion in Section 3.5 that the roaming channel R11 correlates well with the observed ammonia formation in the VLPP experimental conditions.

Another possible explanation for the large amount of hydrogen observed in the experiment of Golden et al. involves heterogeneous MMH decomposition. In fact, a substantial amount of hydrogen formed from the heterogeneous decomposition of MMH was observed in the experiment of Kerr et

al.[12] and the assumed reaction path MMH → CH_4 + H_2 + N_2 agrees well with their experimental measurement. Moreover, their experiment confirmed that ammonia is not formed heterogeneously, at least under their experimental conditions.

3.7 High Pressure Kinetics of CH_4 Formation

Although CH_4 was not observed in Golden et al.'s VLPP experiment, the present study shows that it can be directly formed (via R9) from the MMH decomposition, especially at high temperatures. The pathway CH_3NH_2NH → CH_4 + NH=NH is unlikely to be as important as R9 because of its higher energy barrier. Similar to R11, a roaming radical pathway via

$$CH_3NHNH_2 \rightarrow CH_3 \cdots NHNH_2 \rightarrow CH_4 + NH{=}NH \qquad \text{(R18)}$$

provides another possibly important channel for CH_4 formation. In this pathway, as the C—N bond of MMH stretches, the CH_3 radical may roam around the $NHNH_2$ radical, leading to the barrierless hydrogen abstraction producing CH_4 + NH=NH. This pathway would be expected to produce CH_4 with a rate coefficient that is generally about 1-10% of that for R2.

CH_4 was observed in the experiment of Kerr et al.,[12] who attributed it to the heterogeneous decomposition of MMH, as discussed in Section 3.6. A comparison between the present theory and their experiment is difficult because secondary radical reactions may play an important role under their experimental conditions where the pressures are 0.01-0.04 atm.

3.8 Pressure Dependent Kinetics

Based on the above discussion of the PES for the decomposition of MMH, we can simplify the multi-well, multi-channel PES of MMH decomposition to a single-well, multi-channel one, thereby avoiding the complication of dealing with the multi-well master equation.[34] The contributions of the newly identified reaction channels for MMH decomposition are illustrated in Figure 14, where their pressure dependent reaction rates are shown for pressures ranging from 0.0013 to 100 atm for a temperature of 1000 K. The pressure-dependent rates for the roaming channel, R11, were estimated

with a constant branching ratio of 2%. It is seen that R1, R2, and R11 dominate the MMH decomposition over the entire pressure range and contributions from other channels are negligible.

In our previous study,[8] the experimental data of Kerr et al.,[12] who measured the first-order rate coefficient for R1 at 0.01-0.04 atm and 750-860 K, were well reproduced by the theoretical rate coefficients calculated with $<\Delta E_{down}>=200\ (T/300)^{0.85}$ cm^{-1} for the bath gas N_2. Considering that toluene was in high concentration in the toluene-carrier flow system of Kerr et al., we now also performed calculations for toluene as the bath gas using Lennard-Jones parameters, σ =4.7 Å and ε = 150 cm^{-1}. Given the larger molecular size and the presence of a torsional mode in toluene one expects the $<\Delta E_{down}>$ to be somewhat larger for it. Here we consider two separate values of $<\Delta E_{down}>$ for toluene of $300(T/300)^{0.85}$ and $600(T/300)^{0.85}$ cm^{-1}. Several observations can be made from the comparison, as shown in Figure 15. Overall, the agreement with the experimental data of Kerr et al. is quite reasonable, especially for the calculation at 0.04 atm, with the results for $<\Delta E_{down}>=600(T/300)^{0.85}$ cm^{-1} providing the best fit to the data. However, the theoretical rate coefficients show a pressure fall-off of about a factor or 3 from 0.04 atm to 0.01 atm, while this pressure effect is absent in the experimental data of Kerr et al. It is not clear why this should be the case. Further comparisons between these parameters are not possible in the present study.

In our previous study,[8] the reactions R1 and R2 were found to be insufficient to explain the experimental data of Eberstein and Glassman[5] for the total thermal decomposition rates of MMH at 750-1000 K and atmospheric pressure. Since other channels considered in the present study do not make a major contribution to the MMH dissociation, such a disagreement still holds and suggests that one cannot expect to properly explain the experimental results without considering the effects of secondary radical-molecule and/or radical-radical reactions arising from the MMH decomposition products.

Recently, Li et al.[7] reported rate coefficients for R1 at 0.3-5.2 atm based on NH_2 time-history measurements in shock-tube experiments with argon as the bath gas. The measured rate coefficients follow the same pressure fall-off trends as our previous theoretical predictions.[8] However, a reduction of 40% in the theoretical rate coefficients was needed to reproduce their experimental data.

To understand this discrepancy, we note that the average downward energy transfer used in our previous theoretical rates was based on a fit to the experimental data of Kerr el al., where toluene was used as bath gas. Apparently, a larger $<\Delta E_{down}>$ was needed to model the collisional energy transfer between MMH and toluene, as noted above. For the present study, we have recalculated the rates for Ar as the bath gas and using an average energy down $<\Delta E_{down}>=130(T/300)^{0.85}cm^{-1}$, where the room temperature $<\Delta E_{down}>=130$ cm^{-1} was suggested by Gilbert and Smith.[39] Notably, this value is close to those employed in our studies of C_3H_8 [100 $(T/300)^{0.85}$ cm^{-1}],[47] CH_3CH_2OH [125 $(T/300)^{0.85}$ cm^{-1}],[48] and CH_3CHO [150 $(T/300)^{0.85}$ cm^{-1}],[49] which are of similar size and bond energies. As shown in Figure 16, these revised theoretical predictions agree very well with Li et al.'s experimental data, with discrepancies within the experimental accuracy.

For all the reactions on the PES of MMH decomposition, the calculated fall-off data in the ranges of 400-2500 K and 0.0013-100 atm were fitted with a form that can be readily used in the modeling of MMH pyrolysis and oxidation. These calculations were for N_2 as a bath gas with $<\Delta E_{down}>=120(T/300)^{0.85}cm^{-1}$. The fitting coefficients are listed in Table 1.

4. Conclusions

The decomposition kinetics of monomethylhydrazine was studied with *ab initio* transition state theory based master equation calculations. In addition to the simple N—N and C—N bond fissions, new reaction pathways were identified with energies for all of the stationary points evaluated at the QCISD(T)/CBS//B3LYP/6-311++G(d,p) or QCISD(T)/CBS//CAS+1+2+QC/aug-cc-pVDZ level.

The high pressure rate coefficients were calculated from transition state theory and compared with available experimental data. The roaming channel, MMH → $CH_3NH\ldots NH_2$ → $CH_2NH + NH_3$, appears to be the dominant channel for ammonia formation and estimates of its rate constant agree well with the VLPP experiment of Golden et al.[13] The possible reaction channels on the PES of MMH decomposition for hydrogen formation were identified and found to be insufficient to explain the large amount of hydrogen formation in the experiments. The possible contribution of radical-molecule reactions to hydrogen and ammonia formation was analyzed. The results show that

the hydrogen abstraction channels of MMH by the hydrogen radical cannot be neglected in the VLPP experiments due to their high rate coefficients, while the hydrogen abstraction channels of MMH by the NH_2 radical can be neglected due to their relatively low rate coefficients. Another possible explanation involves the heterogeneous decomposition of MMH, with hydrogen as a major product, while ammonia is absent.

The pressure dependence and product branching in MMH decomposition were obtained from solutions to the master equation. The new theoretical results agree well with the experimental data of Kerr et al.[12] and of Li et al.[7] It was also found that the calculated MMH decomposition rate coefficients are not sufficient to explain the measured total MMH loss rate of Eberstein and Glassman,[5] and that secondary reactions involving MMH and its radicals must be considered. This shortcoming emphasizes the need for a full, detailed reaction mechanism.

Acknowledgements

The work at the Hong Kong Polytechnic University was supported by RGC/ECS (PolyU 5380/13E) and by SRFDP & RGC ERG Joint Research Scheme (M-PolyU509/13). The work at Princeton University was partially supported by the U.S. Army Research Office. The collaboration between Princeton University and the Argonne National Laboratory was facilitated through the Combustion Energy Frontier Research Center sponsored by the Department of Energy. The work at Argonne was supported by the Division of Chemical Sciences, Geosciences, and Biosciences, the Office of Basic Energy Sciences, the U.S. Department of Energy, under contract number DE-AC02-06CH11357. Support at ANL for the roaming radical calculations was provided by the Army Research Office under Grant #W911NF1310251 as part of their Molecular Structure and Dynamics program.

Appendix

In the VLPP experiments of Golden *et al*.,[13, 50-53] bimolecular reactions are suppressed by operating the VLPP reactor at sufficiently low pressures and for sufficiently short residence times. The condition that bimolecular reactions can be neglected is given by[54]

$$f_r = t_r k_M[M] << 1, \quad \text{(A1)}$$

where f_r is the fraction of certain radicals or atoms undergoing bimolecular reactions during the residence time t_r, [M] is the concentration of any reactive species in the system, and k_M is the bimolecular reaction rate coefficient for the radical or atom reacting with M.

In their VLPP study of MMH,[13] Golden et al. did not explicitly specify the residence time or the concentration (pressure) for the experiment, and instead referred readers to references[50-53] for the apparatus and theory of VLPP. Nevertheless, they provided the frequency of gas-wall collisions in the reactor, $\omega = 7.7\times10^3(T/W)^{1/2}$ s^{-1}, where T is the temperature and W is the molar mass of M, and the flow rates $F = 5\times10^{15}$~5×10^{16} molecules/s. From this information we can still estimate the relevant experimental parameters as follows:[50-54]

First, we can obtain the residence time from the relation[54]

$$\omega = Z_w / t_r \quad \text{(A2)}$$

where $Z_w = A_v/A_h$ is the reactor collision number, defined by the ratio of the area of the walls of the reactor to that of the escape aperture. Three reactors were used in the experiments,[52] with three different Z_w =280, 1920, and 22400. Consequently, we can estimate the residence time from the expression

$$t_r = Z_w / \omega = 2.79\times10^{-5} Z_w \quad \text{(A3)}$$

which yields 7.81×10^{-3} s, 5.36×10^{-2} s, and 6.25×10^{-1} s for the three Z_w. These times are consistent with the typical values $10^{-2.5}$ s to 1 s, given in Ref. 54. To derive (A3), we used W=46 for MMH and the typical temperature T=1000 K of the experiment.[13]

We can obtain the concentration via the relation

$$F = [M]cA_h/4, \quad \text{(A4)}$$

where c=146(T/W)$^{1/2}$ m/s=681 m/s is the mean molecular velocity and A_h is the area of the escape aperture. Three apertures were used in the experiments[52] and have areas of 0.74, 8.6, and 78.5 mm^2, respectively. The Clausing factor is about 0.76-0.95 and hence will not cause qualitative errors to (A4). Consequently, we can estimate the concentration from the expression

$$[M] = 4F/cA_h, \quad (A5)$$

which yields 3.97×10^{19}, 3.41×10^{18} and 3.74×10^{17} molecule/m^3, respectively for the three apertures and for $F = 5\times10^{15}$ molecules/s. These concentrations correspond to pressures from 4×10^{-5} to 4×10^{-3} torr, which are consistent with the typical values given in the references [53, 55, 56]. These values should be multiplied by a factor of ten for $F = 5\times10^{16}$ molecules/s.

From Eq. (A1) we can derive a criterion for the critical rate coefficient, $k_{M,cr}$:

$$k_{M,cr}=0.01/t_r[M], \quad (A6)$$

where f_r=0.01<<1 was used to derive (A6). To neglect the influence of a given bimolecular reaction in the VLPP experiment, its rate constant should be smaller than $k_{M,cr}$. Otherwise, the bimolecular reaction must be considered. By using the residence time and the concentration estimated above, we have $k_{M,cr}=4.3\times10^{-15}$~$3.2\times10^{-12}$ cm^3 molecule^{-1} s^{-1}. It is noted that the upper bound $k_{M,cr}=3.2\times10^{-12}$ cm^3 molecule^{-1} s^{-1} was calculated by using the most rigorous conditions, corresponding to $t_r=7.81\times10^{-3}$ s and [M]= 3.74×10^{17} molecule/m^3 (pressure is about 4×10^{-5} torr). Any possible bimolecular reaction in the VLPP of MMH cannot be neglected if its rate is greater than this upper bound.

Table 1. Fitting parameters for calculated rate coefficients for a bath gas of N_2. The rate coefficient is calculated as $k(T)=A(T/T_0)^B\exp(-C/RT) + D(T/T_0)^E\exp(-F/RT)$, T_0=1 K and R=1.987 cal/(K·mol). All the fits are valid from 400 to 2500 K.

Reaction	P(N_2) / atm	A/s^{-1}	B	C/cal mol^{-1}	D/ s^{-1}	E	F/cal mol^{-1}
$CH_3NHNH_2 \rightarrow CH_3NH + NH_2$	0.0013	1.02E+67	-16.73	76800	1.70E+59	-14.10	79000
	0.013	6.64E+58	-13.84	74500	2.72E+50	-11.57	72000
	0.13	1.00E+29	-9.00	45000	2.65E+56	-12.82	74400
	1	2.00E+38	-11.70	48000	1.91E+54	-11.93	74500
	10	3.10E+75	-19.99	75000	1.32E+54	-11.57	76700
	100	1.55E+58	-14.00	71500	2.26E+51	-10.50	77500
	∞	4.55E+23	-2.15	64670			
$CH_3NHNH_2 \rightarrow CH_3 + NHNH_2$	0.0013	4.47E+55	-13.76	75000	3.25E+21	-3.71	73200
	0.013	1.00E+57	-13.84	74990	3.55E+49	-11.57	75000
	0.13	1.00E+40	-8.00	96500	1.30E+56	-13.08	76080
	1	1.51E+53	-16.68	54000	1.10E+55	-12.44	76900
	10	2.08E+35	-15.94	24100	2.69E+53	-11.62	78298
	100	2.39E+08	-0.94	46000	7.94E+48	-10.02	77750
	∞	5.65E+19	-1.12	65640			
$CH_3NHNH_2 \rightarrow CH_2NHNH + H_2$	0.0013	1.26E+52	-13.34	70400			
	0.013	7.21E+52	-13.35	71640	2.82E+47	-11.67	79900
	0.13	1.26E+89	-27.00	73000	4.90E+54	-13.55	74600
	1	2.04E+41	-10.32	65000	5.25E+53	-12.99	75900
	10	6.74E+46	-11.96	67000	1.60E+51	-11.92	77100
	100	1.00E+50	-12.50	70000	3.95E+48	-10.83	79047
	∞	1.46E+06	1.82	57930			
$CH_3NHNH_2 \rightarrow CH_4 + NNH_2$	0.0013	1.35E+49	-12.79	71300	2.68E+21	-4.65	68500
	0.013	1.08E+47	-11.73	71750	3.16E+46	-11.57	78500
	0.13	3.09E+01	1.55	57600	1.05E+52	-12.68	76100
	1	1.00E+52	-16.73	56600	1.48E+54	-12.88	79000
	10	3.16E+30	-6.84	64000	1.76E+50	-11.32	79300
	100	1.14E+48	-11.36	74000	8.87E+52	-11.62	85100
	∞	1.51E+07	2.15	63330			
$CH_3NHNH_2 \rightarrow CH_2=NH + NH_3$ (R10)	0.0013	3.84E+38	-10.51	71300	1.17E+11	-2.54	62000
	0.013	2.66E+41	-10.78	73445	3.98E+39	-10.00	90400
	0.13	2.45E+60	-16.00	82500	7.24E+40	-10.08	75000
	1	9.25E+27	-10.43	48500	8.31E+49	-12.28	79200
	10	6.67E-30	9.06	36000	1.70E+50	-11.89	81550
	100	1.58E+45	-11.30	74200	3.16E+50	-11.47	85400

	∞	5.12E+08	1.27	67350			
$CH_3NHNH_2 \rightarrow CH_3NHN + H_2$	0.0013	1.27E+35	-9.82	68500	2.40E+14	-3.51	68000
	0.013	8.37E+33	-8.83	70255	5.01E+40	-10.00	107000
	0.13	9.70E+80	-24.95	78500	4.17E+42	-10.73	76140
	1	6.31E+88	-31.00	63500	2.34E+46	-11.33	78748
	10	6.03E+39	-10.04	72000	1.05E+50	-11.80	83600
	100	1.86E+44	-11.28	74200	6.92E+48	-11.01	85300
	∞	2.52E+06	2.04	68030			
$CH_3NHNH_2 \rightarrow CH_3NH_2NH$	0.0013	3.47E+50	-12.56	69200	1.41E+55	-13.99	70200
	0.013	6.17E+53	-13.22	71500	6.31E+51	-20.00	35200
	0.13	4.37E+33	-8.88	55100	4.78E+54	-13.19	73500
	1	3.55E+35	-8.70	59000	1.21E+54	-12.75	75000
	10	1.95E+36	-8.03	64000	5.81E+49	-11.20	75000
	100	3.31E+30	-5.94	62950	1.58E+49	-10.69	78500
	∞	1.60E+06	2.05	56040			
$CH_3NHNH_2 \rightarrow CH_3NNH_3$	0.0013	1.56E+34	-8.13	70300	3.37E+59	-15.57	74750
	0.013	5.01E+52	-13.19	73600	6.31E+44	-11.82	65000
	0.13	3.09E+01	1.55	57600	1.00E+52	-12.68	73920
	1	5.37E+48	-12.35	69500	7.92E+53	-12.88	77000
	10	4.03E+39	-9.50	66000	9.94E+51	-11.93	78600
	100	4.39E+34	-7.26	67500	1.46E+51	-11.31	82000
	∞	1.42E+07	1.83	60060			

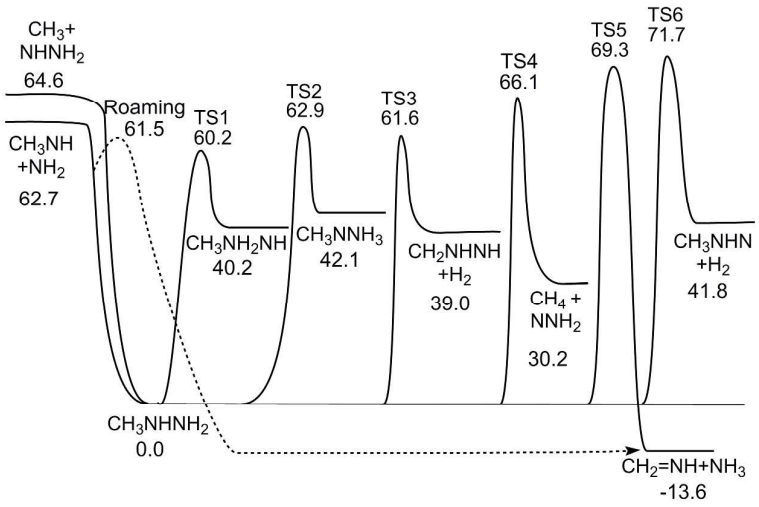

Figure 1. Potential energy surface for CH_3NHNH_2 decomposition at the QCISD(T)/CBS//B3LYP/6-311++G(d,p) level (including ZPE correction). The roaming TS is evaluated at the CASPT2/CBS level relative to $CH_3NH + NH_2$. (Unit: kcal/mol)

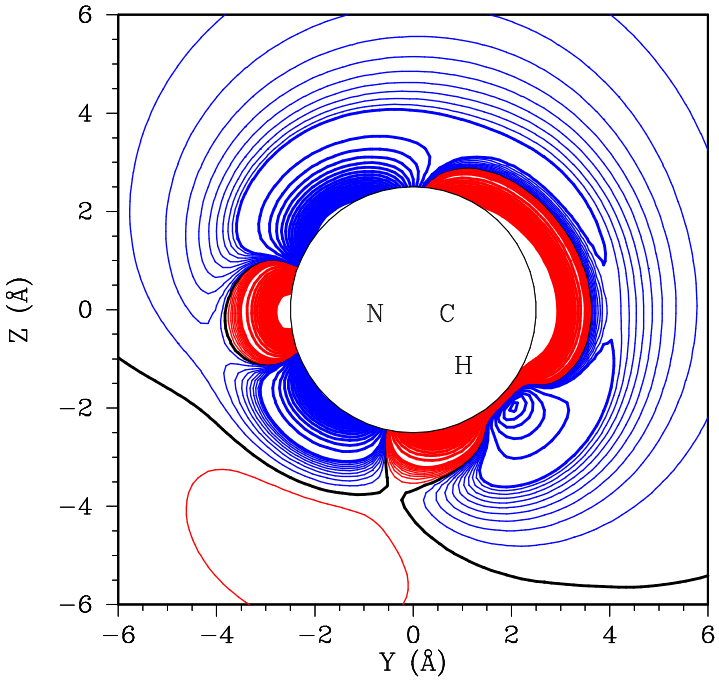

Figure 2. Contour plot of the CASPT2(2e,2o)/aug-cc-pVDZ calculated interaction between CH_3NH and NH_2. The y and z coordinates describe the location of the N in the NH_2 group relative to the center-of-mass of the CH_3NH group, with the CH_3NH group oriented as illustrated and with its NH group oriented out of the plane of the plot. The orientation of the NH_2 group is optimized for each (y,z) point. The blue lines denote attractive contours, while the red lines denote repulsive ones, both with a 0.1 kcal/mol spacing for the first 10 contours and a 1.0 kcal/mol spacing beyond that.

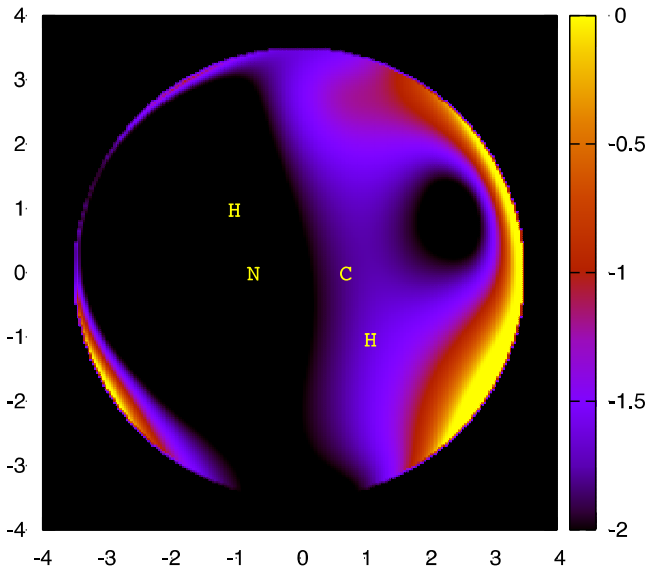

Figure 3. Projection plot of the CASPT2(2e,2o)/aug-cc-pVDZ calculated interaction (in kcal/mol) between CH_3NH and NH_2. For this plot, the potential values for different orientations are projected onto the plane of the plot (with axes in Å) for a fixed separation of 3.5 Å between the N of NH_2 and the center of the CN bond in CH_3NH. The CH_3NH is oriented as indicated, with its NH group in the plane of the plot. The orientation of the NH_2 group is optimized for each point on the plot.

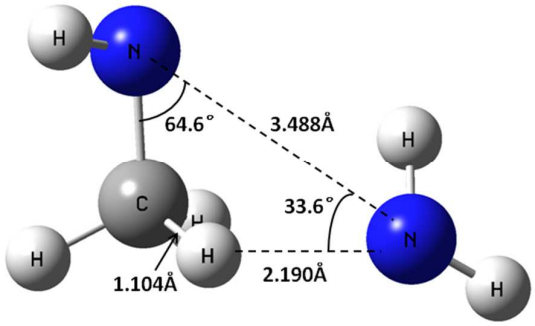

Figure 4. CASPT2(2e,2o)/cc-pVQZ geometry of the saddle point for NH_2 roaming from the N side to the C side of CH_3NH.

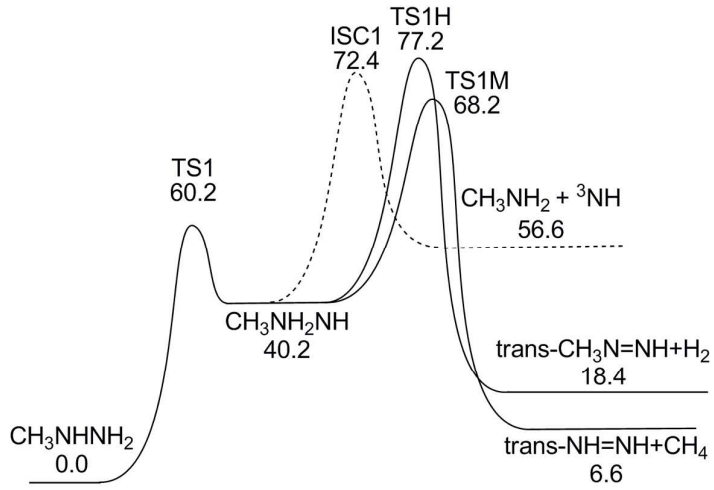

Figure 5. Potential energy surface for CH_3NH_2NH decomposition at the QCISD(T)/CBS//B3LYP/6-311++G(d,p) level (including ZPE correction). (Unit: kcal/mol)

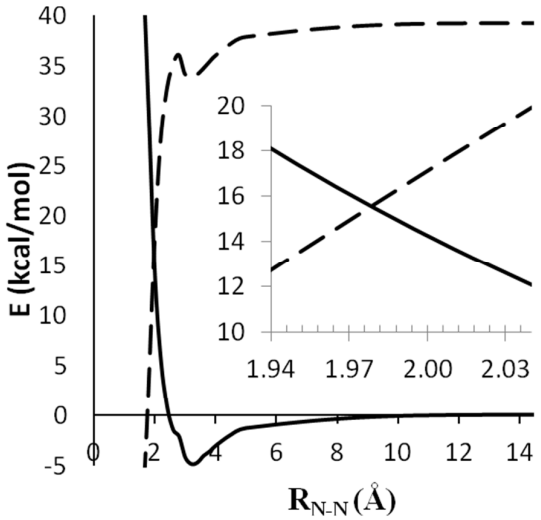

Figure 6. Potential curves for $^1CH_3NH_2NH \rightarrow CH_3NH_2 + {}^1NH$ (dashed) and $^3CH_3NH_2NH \rightarrow CH_3NH_2 + {}^3NH$ (solid) at the CASPT2(2e,2o)/aug-cc-pVDZ level.

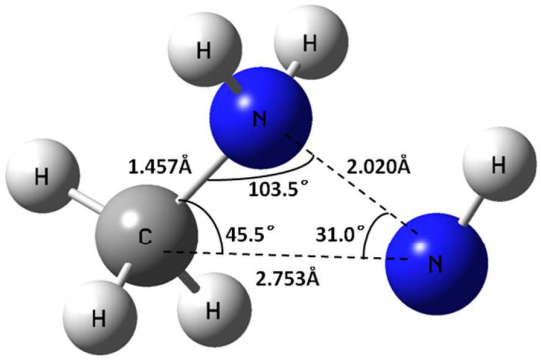

(a)

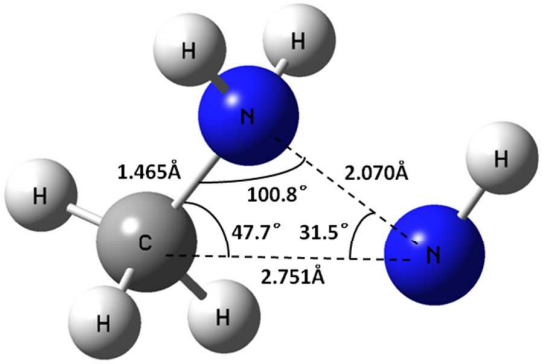

(b)

Figure 7. Geometry of (a) the MSX for $CH_3NH_2NH \rightarrow CH_3NH_2 + NH$ at the CASSCF/6-311++G(d,p) level and (b) the corresponding approximate MSX at the CAS+1+2+QC(2e,2o)/aug-cc-pVDZ level.

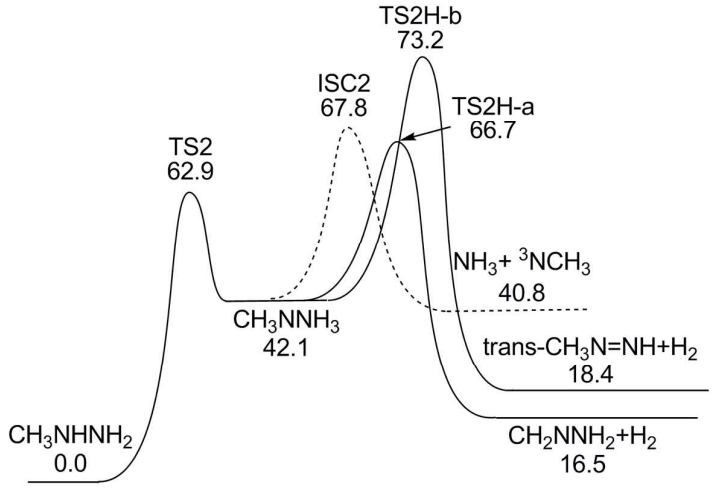

Figure 8. Potential energy surface for CH_3NNH_3 decomposition at the QCISD(T)/CBS//B3LYP/6-311++G(d,p) level (including ZPE correction). (Unit: kcal/mol)

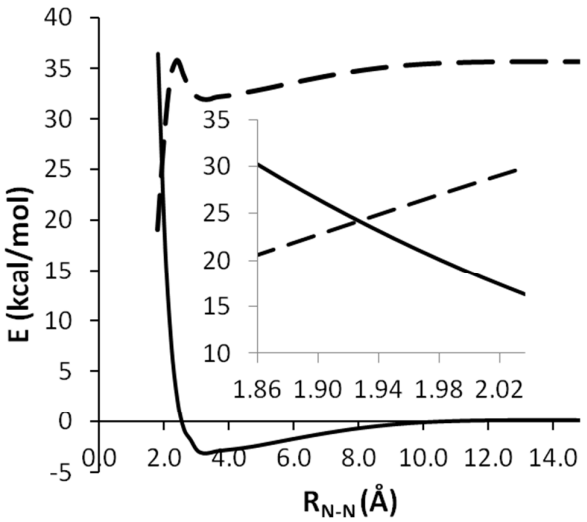

Figure 9. Potential curves for $^{1}CH_3NNH_3 \rightarrow NH_3 + {}^{1}NCH_3$ (dashed) and $^{3}CH_3NNH_3 \rightarrow NH_3 + {}^{3}NCH_3$ (solid) at CASPT2(2e,2o)/aug-cc-pVDZ level.

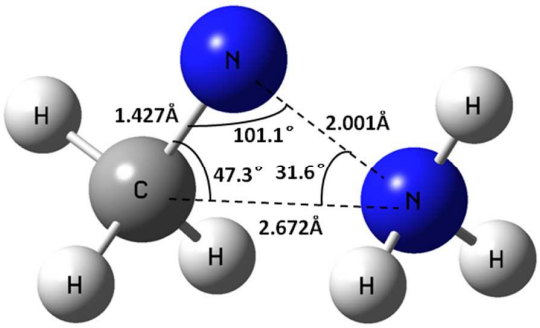

(a)

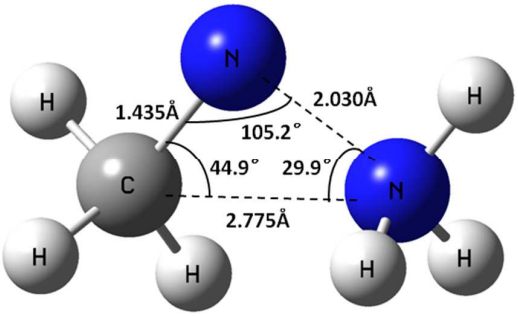

(b)

Figure 10. Geometry of (a) the MSX for $CH_3NNH_3 \rightarrow NH_3 + NCH_3$ at the CASSCF/6-311++G(d,p) level and (b) the corresponding approximate MSX at the CAS+1+2+QC(2e,2o)/aug-cc-pVDZ level.

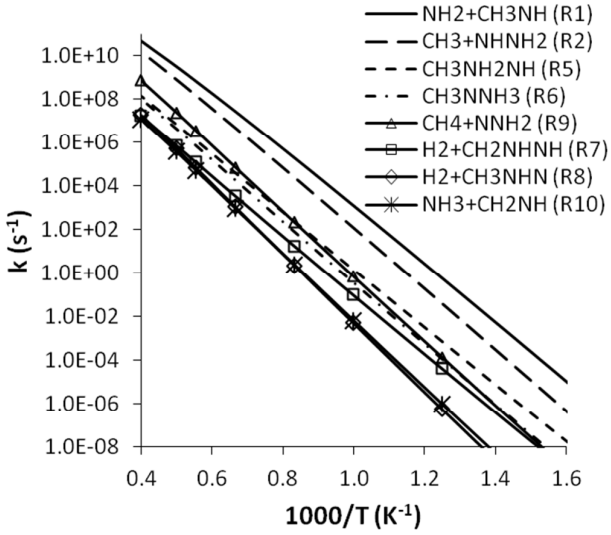

Figure 11. Temperature dependence of the high pressure rate coefficients for MMH dissociation and isomerization.

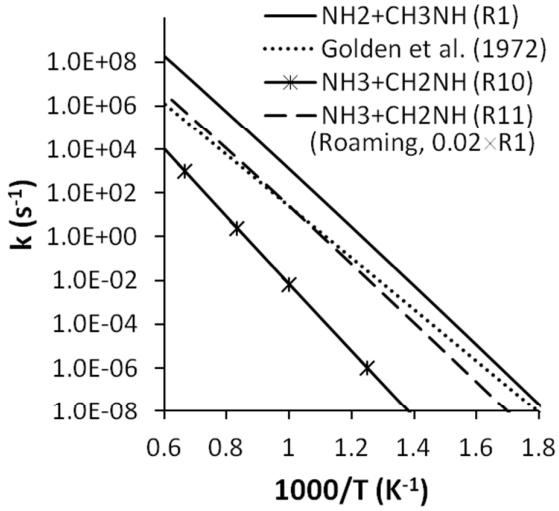

Figure 12. Rate coefficients for ammonia formation from MMH decomposition at different temperatures. The rate coefficient for the roaming channel (R11) was estimated as 2% (the approximate branching ratio near 1000 K) of that for R1.

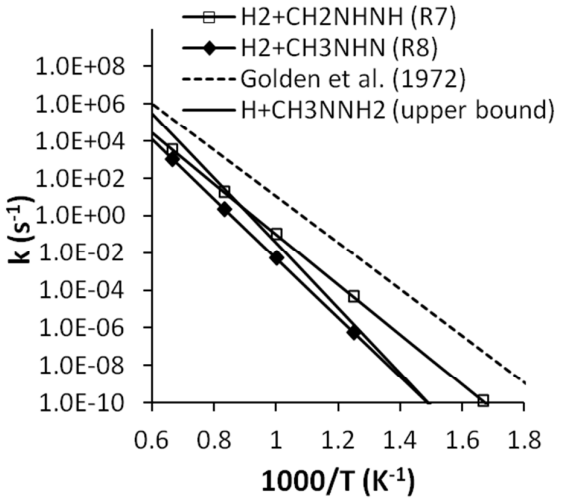

Figure 13. Rate coefficients for hydrogen formation from MMH decomposition at different temperatures.

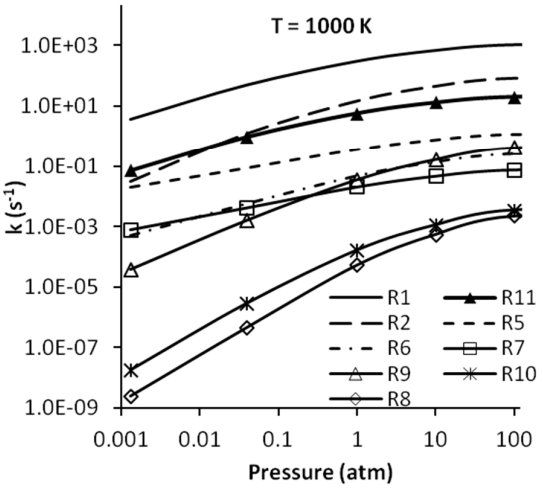

Figure 14. Pressure dependent rate coefficients for the dissociation and isomerization of MMH at a temperature of 1000 K. The rate coefficient for the roaming channel (R11) was estmated as 2% (the approximate branching ratio near 1000 K from 0.001 atm to 100 atm) of that for R1.

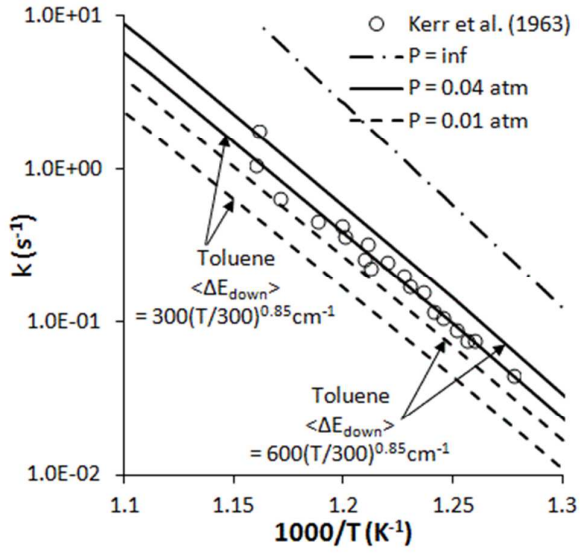

Figure 15. Pressure dependent rate coefficients for R1.

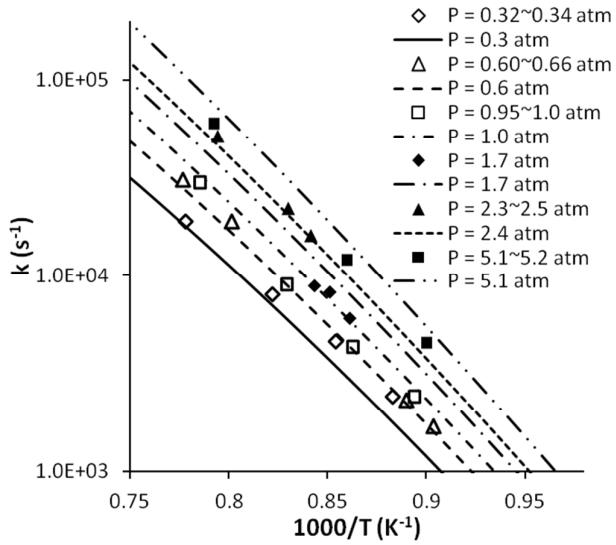

Figure 16. Pressure dependent rate coefficients for R1. Scatter points represent experimental data of Li et al. (2014) and lines the present calcuation data.

Reference

1. L. Catoire, N. Chaumeix and C. Paillard, *J. Propul. Power*, 2004, **20**, 87-92.
2. E. W. Schmidt, *Hydrazine and its derivatives: preparation, properties, applications*, Wiley, New York, 2001.
3. H. Y. Sun and C. K. Law, *J. Phys. Chem. A*, 2007, **111**, 3748-3760.
4. H. Y. Sun, L. Catoire and C. K. Law, *Int. J. Chem. Kinet.*, 2009, **41**, 176-186.
5. I. J. Eberstein and I. Glassman, *Proc. Combust. Inst.*, 1965, **10**, 365-374.
6. R. D. Cook, S. H. Pyun, J. W. Cho, D. F. Davidson and R. K. Hanson, *Combust. Flame*, 2011, **158**, 790-795.
7. S. J. Li, D. F. Davidson and R. K. Hanson, *Combust. Flame*, 2014, **161**, 16-22.
8. P. Zhang, S. J. Klippenstein, H. Y. Sun and C. K. Law, *Proc. Combust. Inst.*, 2011, **33**, 425-432.
9. Y. Georgievskii and S. J. Klippenstein, *J. Chem. Phys.*, 2003, **118**, 5442-5455.
10. S. J. Klippenstein, *J. Phys. Chem.*, 1994, **98**, 11459-11464.
11. S. J. Klippenstein, *J. Chem. Phys.*, 1992, **96**, 367-371.
12. J. A. Kerr, R. C. Sekhar and A. F. Trotman-Dickenson, *Journal of the Chemical Society*, 1963, 3217-3225.
13. D. M. Golden, R. K. Solly, N. A. Gac and S. W. Benson, *Int. J. Chem. Kinetics*, 1972, **4**, 433-448.
14. A. D. Becke, *J. Chem. Phys.*, 1993, **98**, 5648-5652.
15. R. Krishnan, J. S. Binkley, R. Seeger and J. A. Pople, *J. Chem. Phys.*, 1980, **72**, 650-654.
16. T. H. Dunning, *J. Chem. Phys.*, 1989, **90**, 1007-1023.
17. R. A. Kendall, T. H. Dunning and R. J. Harrison, *J. Chem. Phys.*, 1992, **96**, 6796-6806.
18. J. M. L. Martin and O. Uzan, *Chem. Phys. Lett.*, 1998, **282**, 16-24.
19. B. G. Levine, J. D. Coe and T. J. Martinez, *J Phys Chem B*, 2008, **112**, 405-413.
20. D. G. Truhlar and C. A. Mead, *Phys Rev A*, 2003, **68**.
21. A. Farazdel and M. Dupuis, *J. Comput. Chem.*, 1991, **12**, 276-282.
22. M. J. Bearpark, M. A. Robb and H. B. Schlegel, *Chem. Phys. Lett.*, 1994, **223**, 269-274.
23. Q. Cui and K. Morokuma, *Chem. Phys. Lett.*, 1997, **272**, 319-327.
24. J. N. Harvey, M. Aschi, H. Schwarz and W. Koch, *Theor. Chem. Acc.*, 1998, **99**, 95-99.
25. P. J. K. H.-J.Werner, R. Lindh, F. R. Manby, M. Sch¨utz, P. Celani, T. Korona, A. Mitrushenkov, G. Rauhut, T. B. Adler, R. D. Amos, A. Bernhardsson, A. Berning, D. L. Cooper, M. J. O. Deegan, A. J. Dobbyn, F. Eckert, E. Goll, C. Hampel, G. Hetzer, T. Hrenar, G. Knizia, C. K¨oppl, Y. Liu, A. W. Lloyd, R. A. Mata, A. J. May, S. J. McNicholas, W. Meyer, M. E. Mura, A. Nicklass, P. Palmieri, K. Pfl¨uger, R. Pitzer, M. Reiher, U. Schumann, H. Stoll, A. J. Stone, R. Tarroni, T. Thorsteinsson, M.Wang, A. Wolf, *MOLPRO, version 2008.1, a package of ab initio programs*.
26. M. J. Frisch, G. W. Trucks, H. B. Schlegel, G. E. Scuseria, M. A. Robb, J. R. Cheeseman, V. G. Zakrzewski, J. A. Montgomery, R. E. Stratmann, J. C. Burant, S. Dapprich, J. M. Millam, A. D. Daniels, K. N. Kudin, M. C. Strain, O. Farkas, J. Tomasi, V. Barone, M. Cossi, R. Cammi, B. Mennucci, C. Pomelli, C. Adamo, S. Clifford, J. Ochterski, G. A. Petersson, P. Y. Ayala, Q. Cui, K. Morokuma, D. K. Malick, A. D. Rabuck, K. Raghavachari, J. B. Foresman, J. Cioslowski, J. V. Ortiz, B. B. Stefanov, G. Liu, A. Liashenko, P. Piskorz, I. Komaromi, R. Gomperts, R. L. Martin, D. J. Fox, T. Keith, M. A. Al-Laham, C. Y. Peng, A. Nanyakkara, C. Gonzalez, M. Challacombe, P. M. W. Gill, B. Johnson, W. Chen, M. W. Wong, J. L. Andres, C. Gonzalez, M. Head-Gordon, E. S. Replogle and J. A. Pople, *Gaussian 98*, (1998) Gaussian, Inc., Pittsburgh, PA.
27. H.-J. Werner, P. J. Knowles, R. Lindh, M. Schutz, T. K. P. Celani, F. R. Manby, G. Rauhut, R. D. Amos, A. Bernhardsson, A. Berning, D. L. Cooper, M. J. O. Deegan, A. J. Dobbyn, F. Eckert, C. Hampel, G. Hetzer, A. W. Lloyd, S. J. McNicholas, W. Meyer, M. E. Mura, A. Nicklass, P. Palmieri, R. Pitzer, U. Schumann, H. Stoll, A. J. Stone and R. T. Tarroni, *Molpro, Version 2006.1, a package of ab initio programs*, (2006).
28. A. L. L. East and L. Radom, *J. Chem. Phys.*, 1997, **106**, 6655-6674.
29. Q. Cui, K. Morokuma, J. M. Bowman and S. J. Klippenstein, *J. Chem. Phys.*, 1999, **110**, 9469-9482.
30. J. N. Harvey, *Wires Comput Mol Sci*, 2014, **4**, 1-14.
31. S. J. Klippenstein and L. B. Harding, *P Combust Inst*, 2009, **32**, 149-155.
32. C. A. Taatjes, D. L. Osborn, T. M. Selby, G. Meloni, A. J. Trevitt, E. Epifanovsky, A. I. Krylov, B. Sirjean, E. Dames and H. Wang, *J Phys Chem A*, **114**, 3355-3370.
33. S. J. Klippenstein, L. B. Harding, B. Ruscic, R. Sivaramakrishnan, N. K. Srinivasan, M. C. Su and J. V. Michael, *J Phys Chem A*, 2009, **113**, 10241-10259.
34. J. A. Miller and S. J. Klippenstein, *J. Phys. Chem. A*, 2006, **110**, 10528-10544.
35. J. A. Miller and S. J. Klippenstein, *J. Phys. Chem. A*, 2003, **107**, 2680-2692.
36. S. J. Klippenstein, A. F. Wagner, R. C. Dunbar, D. M. Wardlaw, S. H. Robertson and J. A. Miller, *VARIFLEX: Version 2.0m*, (2007).
37. J. A. Miller and S. J. Klippenstein, *Phys. Chem. Chem. Phys.*, 2004, **6**, 1192-1202.
38. H. Wang and M. Frenklach, *Combust. Flame*, 1994, **96**, 163-170.
39. R. G. Gilbert and S. C. Smith, *Theory of Unimolecular and Recombination Reactions*, Blackwell Scientific Publications, 1990.
40. K. Andersson, P. A. Malmqvist and B. O. Roos, *J. Chem. Phys.*, 1992, **96**, 1218-1226.
41. K. P. Huber and G. Herzberg, *Constants of Diatomic Molecules*, Van Nostrand Reinhold, New York, 1979.

42. M. J. Travers, D. C. Cowles, E. P. Clifford, G. B. Ellison and P. C. Engelking, *J. Chem. Phys.*, 1999, **111**, 5349-5360.
43. Y. Georgievskii and S. J. Klippenstein, *J. Phys. Chem. A*, 2003, **107**, 9776-9781.
44. L. B. Harding, Y. Georgievskii and S. J. Klippenstein, *J. Phys. Chem. A*, 2009, **114**, 765-777.
45. L. B. Harding and S. J. Klippenstein, *J. Phys. Chem. Lett.*, 2010, **1**, 3016-3020.
46. H. Y. Sun, P. Zhang and C. K. Law, in *7th US National Technical Meeting of the Combustion Institute*, Atlanta, GA, 2011.
47. R. Sivaramakrishnan, M. C. Su, J. V. Michael, S. J. Klippenstein, L. B. Harding and B. Ruscic, *J. Phys. Chem. A*, 2011, **115**, 3366-3379.
48. R. Sivaramakrishnan, M. C. Su, J. V. Michael, S. J. Klippenstein, L. B. Harding and B. Ruscic, *J. Phys. Chem. A*, 2010, **114**, 9425-9439.
49. L. B. Harding, Y. Georgievskii and S. J. Klippenstein, *J. Phys. Chem. A*, 2010, **114**, 765-777.
50. P. C. Beadle, S. W. Benson, K. D. King and D. M. Golden, *J. Am. Chem. Soc.*, 1972, **94**, 2943-&.
51. P. C. Beadle, D. M. Golden and S. W. Benson, *Int. J. Chem. Kinetics*, 1972, **4**.
52. K. D. King, D. M. Golden, G. N. Spokes and S. W. Benson, *Int. J. Chem. Kinetics*, 1971, **3**.
53. D. M. Golden, N. A. Gac, R. K. Solly and S. W. Benson, *J. Am. Chem. Soc.*, 1972, **94**, 363-&.
54. D. M. Golden, G. N. Spokes and S. W. Benson, *Angew. Chem.-Int. Edit. Engl.*, 1973, **12**, 534-546.
55. S. W. Benson and G. N. Spokes, *J. Am. Chem. Soc.*, 1967, **89**, 2525-&.
56. M. J. Perona and D. M. Golden, *Int. J. Chem. Kinetics*, 1973, **5**, 55-65.